Parcellation of Functional Sub-Regions from fMRI : A Graph Clustering Based Approach

Nandinee Fariah Haq, Sun Nee Tan, Martin J. McKeown, Z. Jane Wang

University of British Columbia, Vancouver, BC, Canada.

Abstract

We propose a framework for parcellating a single brain region-of-interest (ROI) into spatially-contiguous functional sub-regions (subROIs) – each consisting of one or more voxels – based on fMRI connectivity patterns between subROIs and other brain ROIs. First, a functional connectivity network between the voxels in the primary ROI is generated by taking into account the connectivity pattern within the primary ROI and all other ROIs, with a spatial constraint to ensure the spatial continuity of the final subROIs. A community detection algorithm is then applied to the associated adjacency matrix of the connectivity network to parcellate it into functional subROIs. As an illustrative example, the framework was applied to resting state fMRI data from nine healthy subjects to parcellate the putaminal region into two functional subROIs. Training on odd and even time points resulted in more than 98% concurrence of voxels assigned to the same cluster. The relative fraction of voxels assigned to each subROIs was also robust across subjects. As a general tool, the proposed framework has the potential to be integrated into studies investigating subROI alterations in neurological disorders.

Keywords: functional MRI, brain connectivity, community detection, putamen

1. Introduction

Functional magnetic resonance imaging (fMRI) indirectly measures such brain activities by detecting relative alterations in blood oxygen level. For the past three decades, most studies have been carried out focusing on localization of neural activities associated with a variety of cognitive, sensory and

motor tasks. Recent developments in functional neuroimaging have shifted the research focus to investigating and interpreting functional interactions between different brain regions [1, 2, 3, 4, 5, 6, 7]. Study of interactions between brain regions (i.e., brain connectivity) has the potential to provide insights into neural activity related to human behavior and about the alterations of these connectivities in neurodegenerative diseases [8, 9, 10]. While connectivity studies can be targeted at exploring task-related interactions among brain regions, similar studies can be carried out on resting-state fMRI as well, investigating the spontaneous interaction between brain regions without the subject concentrating on a specific task [11, 12, 13]. Resting state connectivity studies are particularly useful when it is difficult for the subject to actively engage in sensory, motor or cognitive tasks (e.g., due to dementia).

Connectivity studies can be carried out at the voxel level, generally requiring spatial transformation of all brain volumes to a common template – a process which is susceptible to misregistration. Moreover, voxel-based analysis deals with a large number of variables, often making it computationally intractable. Therefore many studies opt for regions-of-interest (ROIs)-based connectivity analysis. ROI-based analysis reduces the computational complexity and does not necessarily require spatial transformation. However, the definition of an ROI requires careful consideration. Functional ROIs can be derived from anatomical ROIs, where images are mapped to a standard brain template by matching topographic landmarks [14] or they can be derived directly from the functional connectivities between brain voxels [15].

In some cases, such as the putamen in the basal ganglia, there may exist several functional sub-regions-of-interest (subROIs) within one anatomically-defined ROI [16, 17, 18, 19, 20, 21]. Exploration of the connectivity patterns of the functional subROIs within the striatal structures of the putamen and caudate could be of substantial importance in understanding basal ganglia disorders such as Parkinson's disease, Huntington's disease, and Tourette's syndrome [20]. Moreover, parcellation of basal ganglia subROIs could play an important role in developing more detailed models of whole-brain connectivity networks [22] and in evaluating hypotheses about healthy aging [23] and evolving cortical-basal ganglia circuitry in typical development [24].

In this paper, we propose a framework to define functional subROIs within the putaminal region by exploring functional connectivities between themselves and with other ROIs. Extensive neuroscience research has concluded that the putamen is functionally sub-divided into at least two subROIs, namely- dorsolateral striatum (DLS) which is associated with habitual con-

2

trol and dorsomedial striatum (DMS) which is associated with goal-oriented control [25]. Functionally, in the basal ganglia-cortical loops in animals, these subROIs are connected to different cortices with distinct connectivity patterns [25, 26]. The dissimilarity in the connectivity pattern of the subROIs with other cortical ROIs motivates us to develop a data-driven approach for functional subROI parcellation in the putamen.

Several studies have been proposed that utilize data-driven approaches to sub-divide a given ROI into functional subROIs. One approach is clustering based on features, for example, the Pearson's pairwise correlation between each voxel's timecourse within the ROI with that of other brain regions, and then a clustering algorithm is applied to divide the voxels into several sub-groups [27, 28, 29]. However, most clustering methods are very sensitive to outliers, requiring extensive preprocessing and denoising steps to obtain spatially contiguous results. For example, some clustering methods incorporate component analysis [30], spectral analysis [31], fitting of regressors [27, 29] or intra-session pre-clustering [32] as a pre-processing step prior to clustering, while other methods require repetitive applications of algorithms to find spatially contiguous ROIs [16]. Another approach, based on graph theory, represents each voxel within the ROI as a node in a graph. This graph is then divided into subROIs using modularity detection [20] or a normalized cut approach [33]. However, due to head movement and other artifacts, fMRI data of non-spatially contiguous voxels may be inappropriately grouped together.

Many current parcellation methods do not impose spatial continuity and therefore in such cases, graph-theory based approaches do not, in general, generate spatially contiguous subROIs, as would be expected from the underlying physiology inferred from animal models. Moreover, these approaches frequently only incorporate the connectivity between the voxels within the ROI disregarding their connectivity patterns with other brain regions. Recently Zhang *et al.* [34] proposed a subROI parcellation technique based on a spatially regularized regression model that incorporates the spatial information along with the connectivity patterns with other ROIs. However, the voxel-connectivities within the ROI were not considered. Moreover, the method considers only one reference region at a time in the optimization model rather than incorporating the combined effect from all reference regions. Furthermore, the robustness of the method highly depends on its optimization parameters making tuning the parameters a challenging task. Therefore there is still a need for a complete framework for functional subROI parcellation that can incorporate both inter- and intra-ROI connectivity

patterns while imposing spatial continuity for subROIs.

Here, we propose a data-driven graph-theoretic framework for parcellation of the putaminal region into two spatially contiguous functional subROIs. We propose a connectivity network generation approach that incorporates the connectivities of the target ROI (in this case, the putamen) voxels with other cortical ROIs along with their spatial distances and the connectivities between the putaminal voxels themselves. A community detection based approach is then adopted to sub-divide the connectivity network into two spatially contiguous subROIs. Our proposed approach imposes the spatial continuity on subROIs which is often ignored in the literature. This approach also combines the effect of connectivity patterns of the putaminal region within itself and with the other brain regions, hence generating a complete representation of the overall connectivity characteristics inside the putamen. Although the framework is developed for putaminal parcellation, it is generally applicable to other brain region parcellation problems.

2. Method

In this section, we describe the proposed framework for separating a given ROI into two or more functionally and spatially contiguous subROIs. Throughout this paper, the term *target ROI* is used to denote the ROI which we want to divide into subROIs, and *reference ROIs* is used to denote other brain ROIs which interact with the target ROI. The proposed framework can be divided into two main steps: first, we generate a connectivity network for the target ROI by taking into account the connectivity between voxels within the target ROI, their connectivity with the reference ROIs and their spatial distances. In the next step, we incorporate a community detection approach to divide the target ROI into the functional subROIs.

2.1. Connectivity Network Generation

We formulated the parcellation of subROIs in the putamen as a weighted-graph clustering problem in the voxel space. Based on prior work, the putaminal region can be divided into at least two functional subROIs, namely the dorsolateral striatum (DLS) and dorsomedial striatum (DMS). To formulate the parcellation of functional subROIs as a graph clustering problem, a network is generated where each voxel within the putaminal region is represented by a node in the graph and the edge weights between them are derived from brain connectivity patterns. The generation of the network, $\mathcal{G}$, is graphically
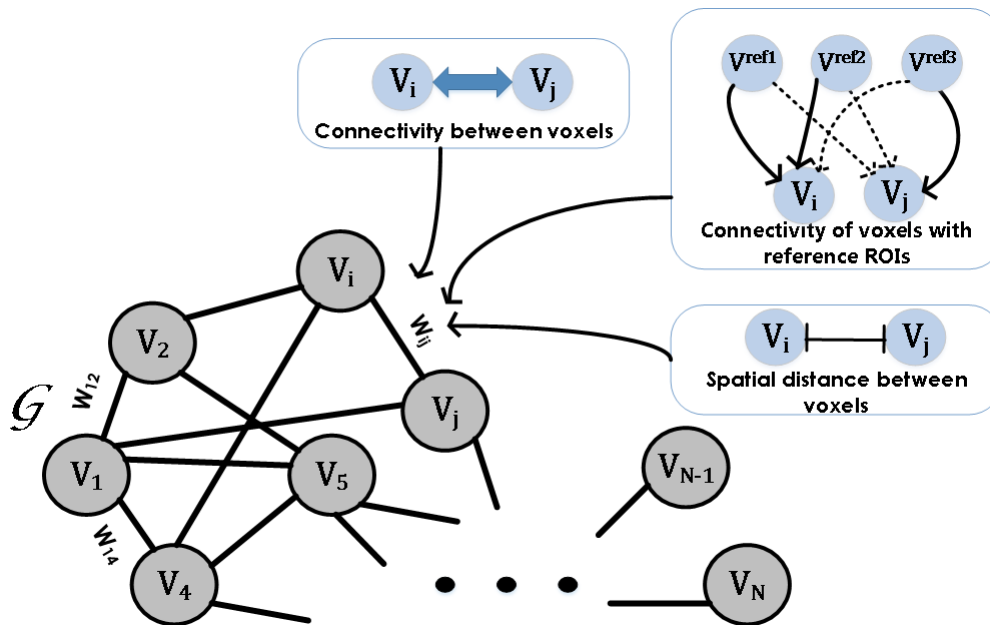
Figure 1: Illustration of the putamen connectivity network generation.

shown in Fig. 1. V_i and V_j denote the ith and j^{th} voxels in the target ROI, which are represented by the nodes in the graph $\mathcal{G}$, and V^{ref} denote the voxels from the reference regions. For any two voxels V_i and V_j in the graph, the edge weight between them, $\mathcal{W}_{ij}$, is calculated by taking into account the following three factors:

- the connectivity between voxels within the target ROI;

- the connectivity between each voxel within the target ROI and other reference ROIs;

- the spatial (Euclidian) distances between voxels.

To elaborate, the division of functional subROIs depends on their dissimilarity in connectivity with other brain regions. According to prior neuroanatomical knowledge, different subROIs in the putaminal region have different connectivity patterns with other brain regions. For this work, we considered three reference regions: the sensorimotor area (SMA), the orbitofrontal gyrus (OF), and the cingulate gyrus (CG), as these are reported to have significant differences in their connectivity patterns with the putamen subROIs. The SMA tends to have a strong connectivity with the DLS
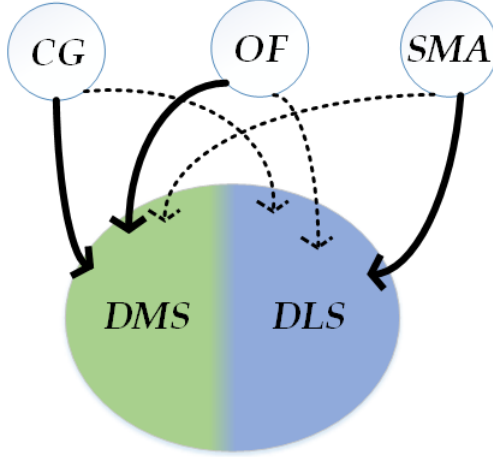
5

Figure 2: Connectivity patterns of functional subROIs in the putaminal region with sensorimotor cortex (SMA), cingulate gyrus (CG) and orbitofrontal gyrus (OF). The solid lines denote strong connectivity and the dotted lines denote weak connectivity.

and weaker connectivity with the DMS, whereas the OF and CG cortices show strong connectivity with the DMS and weaker connectivity with the DLS [20]. Fig. 2 shows the connectivity pattern of the subROIs with the reference ROIs. The edge weight between two target ROI voxels in the generated graph $\mathcal{G}$ should reflect this dissimilarity of connectivity patterns with the reference regions. Therefore we propose generating the weight term between two target ROI voxels originating from the connectivity patterns with the reference regions as follows:

$$W_{ij}^{ref} = 1 - \frac{\sum_{m=1}^{M} |C_{m,i}^{ref} - C_{m,j}^{ref}|}{M}; \quad i \neq j. \tag{1}$$

Here, W_{ij}^{ref} is the weight term generated when taking into account differences in connectivity patterns of the reference ROIs with the target ROI voxels i and j. $C_{m,i}^{ref}$ and $C_{m,j}^{ref}$ are the connectivities between reference ROI m and target ROI voxels i and j respectively. M is the total number of reference ROIs. To remove the effect of other reference ROIs while calculating $C_{m,i}^{ref}$, we defined the connectivity between reference m and target ROI voxel i as the absolute value of partial correlation coefficient, $\rho_{partial}$ between the temporal signal of the ith voxel, y_i, and the average temporal signal of the mth reference ROI, y_m^{ref}, controlling for the average temporal signals of the remaining (M-1) reference ROIs as follows:

$$C_{m,i}^{ref} = |\rho_{partial}(y_i, y_m^{ref}|y_1^{ref}, ..., y_{m-1}^{ref}, y_{m+1}^{ref}, ..., y_M^{ref})|. \tag{2}$$

Eqn. 1 is based on the idea that if voxels V_i and V_j have similar connectivity with all the reference ROIs, then these voxels are similar and hence the edge connecting them in $\mathcal{G}$ should have the weight proportional to the similarity. If V_i and V_j are both strongly connected with all the reference regions, their edge weight W_{ij}^{ref} should be large. A similar scenario is when both voxels are weakly connected with all the reference regions. This also means that the task voxels share similar connectivity patterns with reference regions and hence their edge weight W_{ij}^{ref} should be large as well. Therefore the edge weight term originating from the connectivities with reference ROIs, W_{ij}^{ref}, takes into account the differences between the connectivities with the reference ROIs. As can be seen from Eqn. 1, the second term on the right side is the mean of the differences in connectivities over all the reference regions. If V_i and V_j both have strong connectivity with two reference ROIs and weak connectivity with all other reference ROIs, it means V_i and V_j share similar connectivity patterns with all the reference ROIs. Then the difference in their connectivities with references are low, and the second term on the right side of Eqn. 1 is low, as a result W_{ij}^{ref} is high. On the other hand, when V_i and V_j have different connectivity patterns (i.e., V_i is strongly connected with some reference ROIs whereas V_j is weakly connected with those reference ROIs, and vice versa), then the second term on the right side of Eqn. 1 is high, as a result W_{ij}^{ref} is low. W_{ij}^{ref} takes values in the range $[0, 1]$. $W_{ij}^{ref} = 1$ if V_i and V_j share exactly the same connectivity pattern ($C_{m,i}^{ref} = C_{m,j}^{ref}$ for all m), and $W_{ij}^{ref} = 0$ if V_i and V_j share exactly the opposite connectivity pattern ($|C_{m,i}^{ref} - C_{m,j}^{ref}| = 1$ for all m).

The connectivity between the target ROI voxels and their spatial positions should also influence the edge weights between them. The final edge weight between voxels V_i and V_j is calculated by multiplying a factor W_{ij}^{target} with W_{ij}^{ref}. W_{ij}^{target} incorporates the connectivities between voxels in the target ROI and their Euclidean spatial distances, and is applied such that it multiplies or decreases W_{ij}^{ref}, based on the actual connectivities between V_i and V_j. The final edge weight, $\mathcal{W}_{ij}$ is calculated as:

$$\mathcal{W}_{ij} = \begin{cases} 0 & \text{for } i = j \\ W_{ij}^{target} \times W_{ij}^{ref} & \text{for } i \neq j \end{cases} \tag{3}$$
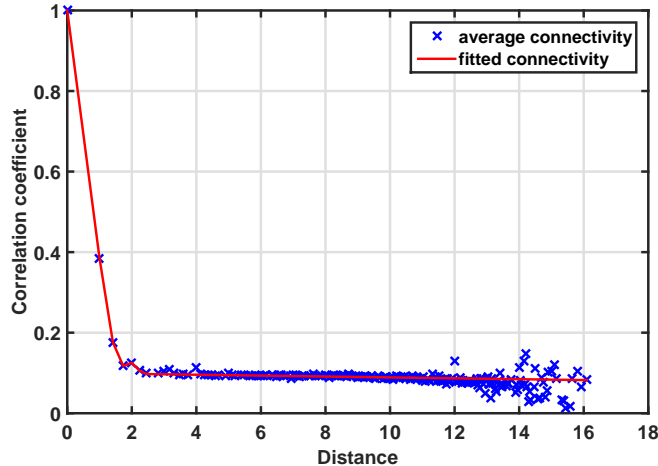
Figure 3: Pair-wise Voxel connectivity pattern against their Euclidean distance between voxels within the target ROI. The blue crosses are the average correlation coefficients between voxels and the red line is the fitted curve to represent the connectivity change with increasing distance (i.e., in terms of their Euclidean distance in mm).

Here $\mathcal{W}_{ij}$ is set to zero when $i = j$ to eliminate self-loops in $\mathcal{G}$.

To incorporate the spatial information and connectivities within the target ROI in the final edge weight, we plotted the average pair-wise connectivity within the target ROI against their spatial distances. We used Pearson's pair-wise correlation coefficient to define connectivity between two voxels within the target ROI. A curve is then fitted to best represent the internal connectivity pattern in the target ROI with their Euclidean distances. The fitted connectivity pattern vs. their Euclidean distance is shown in Fig. 3. It can be seen that the average connectivity decreases rapidly with the distance, and almost saturates at a fixed value afterward. The weighting term incorporating the connectivity pattern within the target ROI is defined as:

$$W_{ij}^{target} = \delta_D^T(||\mathbf{r}_i - \mathbf{r}_j||) \times C^{target}(||\mathbf{r}_i - \mathbf{r}_j||); \quad i \neq j \tag{4}$$

where $C^{target}(d)$ denotes the fitted value of the correlation coefficient at a distance d. $\mathbf{r}_i$ and $\mathbf{r}_j$ denote the spatial location of voxels V_i and V_j respectively and $||\mathbf{r}_i - \mathbf{r}_j||$ denotes the Euclidean distance between them. δ_D^T is introduced to impose thresholding on the linkage between spatially distant voxels, and is defined as:

$$\delta_D^T(d) = \begin{cases} 1, & \text{if } d \leq T \\ 0, & \text{otherwise} \end{cases}$$

This thresholding ensures that spatially distant voxels do not share edges in the generated network $\mathcal{G}$ and hence are well separated. The final weight of the edge between V_i and V_j is calculated as follows:

$$
\begin{aligned}
\mathcal{W}_{ij} =& W_{ij}^{target} \times W_{ij}^{ref}; \quad i \neq j \\
\Rightarrow \mathcal{W}_{ij} =& \delta_D^T(||\mathbf{r}_i - \mathbf{r}_j||) \times C^{target}(||\mathbf{r}_i - \mathbf{r}_j||) \\
& \times \left[1 - \frac{\sum_{m=1}^M |C_{m,i}^{ref} - C_{m,j}^{ref}|}{M} \right]; \quad i \neq j
\end{aligned}
\tag{5}
$$

The curve in Fig. 3 incorporates the connectivity pattern as a function of the distance within the target ROI and the total edge weight should also follow such a pattern if plotted against the distance. Therefore the final weight of the edge between V_i and V_j is calculated as the multiplication of the two terms W_{ij}^{target} and W_{ij}^{ref}. If two voxels are highly connected based on their connectivities with reference ROIs but are spatially distant, W^{ref} is higher between them. However, since they are spatially distant, there should be less weight to the edges connecting them. So their final edge weight is decreased by the multiplying term W^{target} to generate the final weight $\mathcal{W}$. W^{target} decreases rapidly with the distance and goes to zero beyond the threshold T. This ensures that the edge weights are spatially consistent and distant voxels are well-separated or disconnected. At the boundary between two subROIs, W^{target} generates a higher value. However W^{ref} generates a low value as the voxels in consideration are functionally different and shows different connectivity pattern with the reference ROIs, and hence the final edge weight $\mathcal{W}$ decreases, as can be seen from Eqn. 5. $\mathcal{W}$ takes the values within the range $[0, 1]$.

2.2. Community Detection

After generating the connectivity network, we divided the network $\mathcal{G}$ into $\mathcal{K}$ subROIs. To determine the subROIs, we implemented a recently proposed community detection algorithm [35] that divides the network based on the ratio of the eigenvectors of the adjacency matrix. This algorithm has shown to outperform other methods for graphs with well-known structures and is computationally faster, making it a better choice for practical applications.

We start by generating the adjacency matrix, $\mathcal{A}$, for the network, $\mathcal{G}$, as follows:

$$\mathcal{A} = \begin{bmatrix} \mathcal{W}_{11} & \mathcal{W}_{12} & \mathcal{W}_{13} & \dots & \mathcal{W}_{1N} \\ \mathcal{W}_{21} & \mathcal{W}_{22} & \mathcal{W}_{23} & \dots & \mathcal{W}_{2N} \\ \vdots & \vdots & \vdots & \ddots & \vdots \\ \mathcal{W}_{N1} & \mathcal{W}_{N2} & \mathcal{W}_{N3} & \dots & \mathcal{W}_{NN} \end{bmatrix} \tag{6}$$

where N is the total number of nodes in the network $\mathcal{G}$. To eliminate self-loops, the diagonal elements are set to zero, i.e., $\mathcal{W}_{ii} = 0$ for $i = 1, 2, ..., N$ as shown in Eqn. 3. Moreover, here we consider undirected graph only, hence the adjacency matrix is symmetric, i.e. $\mathcal{W}_{ij} = \mathcal{W}_{ji}$. After considering these conditions, we have the final adjacency matrix as:

$$\mathcal{A} = \begin{bmatrix} 0 & \mathcal{W}_{12} & \mathcal{W}_{13} & \dots & \mathcal{W}_{1N} \\ \mathcal{W}_{12} & 0 & \mathcal{W}_{23} & \dots & \mathcal{W}_{2N} \\ \mathcal{W}_{13} & \mathcal{W}_{23} & 0 & \dots & \mathcal{W}_{3N} \\ \vdots & \vdots & \vdots & \ddots & \vdots \\ \mathcal{W}_{1N} & \mathcal{W}_{2N} & \mathcal{W}_{3N} & \dots & 0 \end{bmatrix} \tag{7}$$

After generating the adjacency matrix, the community detection algorithm divides the network into $\mathcal{K}$ distinct communities by sequential execution of a few steps. First, $\mathcal{K}$-leading eigenvalues of $\mathcal{A}$ are calculated. Let the $\mathcal{K}$ leading eigenvalues are $\lambda_1 > \lambda_2 > ... > \lambda_{\mathcal{K}}$ and the corresponding unit-norm eigenvectors are $\mathcal{V}_1, \mathcal{V}_2, ..., \mathcal{V}_{\mathcal{K}}$ respectively. The matrix $\mathcal{R}^{N \times \mathcal{K}-1}$ is generated by taking entry-wise ratio of the eigenvectors as follows:

$$\mathcal{R} = \begin{bmatrix} \frac{\mathcal{V}_2(1)}{\mathcal{V}_1(1)} & \frac{\mathcal{V}_3(1)}{\mathcal{V}_1(1)} & \cdots & \frac{\mathcal{V}_{\mathcal{K}}(1)}{\mathcal{V}_1(1)} \\ \frac{\mathcal{V}_2(2)}{\mathcal{V}_1(2)} & \frac{\mathcal{V}_3(2)}{\mathcal{V}_1(2)} & \cdots & \frac{\mathcal{V}_{\mathcal{K}}(2)}{\mathcal{V}_1(2)} \\ \vdots & \vdots & \ddots & \vdots \\ \frac{\mathcal{V}_2(N)}{\mathcal{V}_1(N)} & \frac{\mathcal{V}_3(N)}{\mathcal{V}_1(N)} & \cdots & \frac{\mathcal{V}_{\mathcal{K}}(N)}{\mathcal{V}_1(N)} \end{bmatrix} \tag{8}$$

The nodes of the graph $\mathcal{G}$ are then clustered into $\mathcal{K}$ communities by applying the k-means algorithm onto $\mathcal{R}$. The k-means algorithm is repeated 100 times to ensure that a local minimum is obtained.
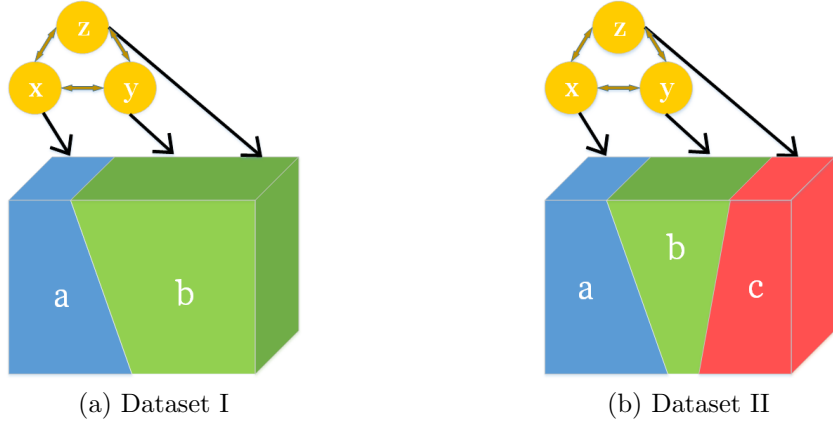
(a) Dataset I   (b) Dataset II

Figure 4: Illustration of the synthetic data generation process. x, y and z are three interconnected reference regions. (a) Dataset I: The cubic volume consists of two sub-regions a and b, where a has strong connectivity with x and b has strong connectivity with y and z. (b) Dataset II: The cubic volume consists of three sub-regions a, b and c, where a has strong connectivity with x, b has strong connectivity with y and c has strong connectivity with z.

3. Datasets

We compared the performance of the proposed framework with other methods described in the literature using two sets of synthetic data before applying it to a real fMRI dataset. The datasets used in this paper are discussed in this section.

3.1. Synthetic Datasets

To demonstrate the performance of the proposed method, we generated synthetic datasets and applied the proposed framework to extract the sub-ROIs. To demonstrate the applicability of the framework in extracting different numbers of subROIs, here we applied the framework to two sets of synthetic data. Fig. 4 shows the synthetic data generation process and Table 1 summarizes the datasets generated.

3.1.1. Dataset I

The first synthetic dataset is a $10\times10\times10$ cubic volume $\mathcal{V}$ divided into two spatially contiguous sub-regions- a and b. The target region consists of 1000 voxels and the sub-regions a and b consists of 440 and 560 voxels respectively. To ensure the synthetic dataset is compliant with real fMRI

Table 1: Description of the synthetic datasets. Each dataset consists of 50 sets of data.

Dataset	Description	Signal to Noise Ratio (SNR)
IA	Two subROIs, no outliers	$\text{SNR}_{data} = 6$ dB
IB	Two subROIs, 100 outliers in each ROI	$\text{SNR}_{data} = 6$ dB, $\text{SNR}_{outlier} = $ -3 dB
IC	Two subROIs, 100 outliers in each ROI	$\text{SNR}_{data} = 6$ dB, $\text{SNR}_{outlier} = $ -10 dB
IIA	Three subROIs, no outliers	$\text{SNR}_{data} = 6$ dB
IIB	Three subROIs, 50 outliers in each ROI	$\text{SNR}_{data} = 6$ dB, $\text{SNR}_{outlier} = $ -3 dB
IIC	Three subROIs, 50 outliers in each ROI	$\text{SNR}_{data} = 6$ dB, $\text{SNR}_{outlier} = $ -10 dB

conditions in our problem, three reference regions, x, y and z, are generated and the signals in two sub-regions, a and b, are generated such that these sub-regions have different connectivity patterns with each of the reference regions. Each reference region consists of 240 voxels. The temporal signals of the reference ROIs and the target ROI are 240-time point long and are generated using the following model:

$$
\begin{aligned}
r_x &= \theta_1 m_s + (1 - \theta_1)l_s + \epsilon_1 \\
r_y &= \theta_2 n_s + (1 - \theta_2)l_s + \epsilon_2 \\
r_z &= \theta_3 n_s + (1 - \theta_3)l_s + \epsilon_3 \\
x_a &= \alpha[\theta_a m_s + (1 - \theta_a)l_s] + (1 - \alpha)k_s + \epsilon_a \\
x_b &= \beta[\theta_b n_s + (1 - \theta_b)l_s] + (1 - \beta)r_s + \epsilon_b \\
l_s, m_s, n_s, k_s, r_s &\sim \mathcal{N}(0, 1) \\
\epsilon_1, \epsilon_2, \epsilon_3, \epsilon_a, \epsilon_b &\sim \mathcal{N}(0, \sigma_N^2) \\
\theta_1, \theta_2, \theta_3, \theta_a, \theta_b, \alpha, \beta &\sim \mathcal{U}[0.5, 0.9].
\end{aligned}
\tag{9}
$$

Here r_x, r_y and r_z denote signals in the reference regions x, y and z respectively. The temporal signals for the reference regions are generated from three source signals- l_s, m_s and n_s. The source signals are generated from a normal distribution with zero mean and unit variance, and to comply with real fMRI signals, a temporal Gaussian smoother is also applied on the source signals. Signals for the reference region x are generated from the source signals l_s and m_s, whereas signals for y and z are generated from l_s and n_s. Since different brain regions interact with each other, here the source signal l_s is used to generate all three reference region signals to ensure the reference regions in the synthetic dataset are also internally connected.

To be similar with real fMRI data from the putamen, signals for sub-

regions a and b are generated such that one sub-region has strong connectivity with one reference region and the other sub-region has connectivity with other two reference regions. As can be seen from Eqn. 9, the signal for the sub-region a, x_a, is correlated with r_x, whereas the signal for the sub-region b, x_b, is correlated with r_y and r_z. The added noise, ϵ, follows a zero-mean Gaussian distribution and the variance σ_N^2 is calculated based on the signal-to-noise ratio (SNR).

To observe the effect of outliers, we generated three datasets using this data generation process (setup A, B and C). The first synthetic dataset (Dataset-IA) is generated by using a fixed SNR ($\text{SNR}_{data} = 6$ dB) for all the voxels. For Dataset-IB and IC, we included some outliers in the dataset. To incorporate this outlier effect, we randomly chose 100 voxels in each of the sub-regions a and b and used a lower SNR ($\text{SNR}_{outlier} = -3$ dB for Dataset-IB and $\text{SNR}_{outlier} = -10$ dB for Dataset-IC) to generate the signals for those voxels. These 200 voxels serve as the outliers and the rest of the voxels are generated using $\text{SNR}_{data} = 6$ dB as Dataset-IA. The procedure is repeated 50 times so that Dataset-IA, IB and IC each contains 50 sets of data.

3.1.2. Dataset II

To generate Dataset-II, the $10 \times 10 \times 10$ cubic volume $\mathcal{V}$ is divided into three spatially contiguous sub-regions- a, b and c. The sub-regions a, b and c contains 330, 340 and 330 voxels respectively. The reference regions, x, y and z, are generated similarly as described in the previous section and the signals in a, b and c are generated using the following model:

$$
\begin{aligned}
r_x &= \theta_1 m_s + (1 - \theta_1)l_s + \epsilon_1 \\
r_y &= \theta_2 n_s + (1 - \theta_2)l_s + \epsilon_2 \\
r_z &= \theta_3 k_s + (1 - \theta_3)l_s + \epsilon_3 \\
x_a &= \alpha[\theta_a m_s + (1 - \theta_a)l_s] + (1 - \alpha)t_s + \epsilon_a \\
x_b &= \beta[\theta_b n_s + (1 - \theta_b)l_s] + (1 - \beta)r_s + \epsilon_b \qquad (10) \\
x_c &= \gamma[\theta_c k_s + (1 - \theta_c)l_s] + (1 - \gamma)q_s + \epsilon_c \\
l_s, m_s, n_s, k_s, t_s, r_s, q_s &\sim \mathcal{N}(0, 1) \\
\epsilon_1, \epsilon_2, \epsilon_3, \epsilon_a, \epsilon_b, \epsilon_c &\sim \mathcal{N}(0, \sigma_N^2) \\
\theta_1, \theta_2, \theta_3, \theta_a, \theta_b, \theta_c, \alpha, \beta, \gamma &\sim \mathcal{U}[0.5, 0.9].
\end{aligned}
$$

Here r_x, r_y and r_z denote signals in the reference regions and x_a, x_b and x_c denote the signals in the three sub-regions. The temporal signals for

13

the reference regions are generated from four source signals- l_s, m_s, n_s and k_s, where the source signal l_s is used to generate all three reference region signals to ensure the reference regions are internally connected. Dataset-IIA is generated by using a fixed SNR ($\text{SNR}_{data} = 6$ dB) for all the voxels. For Dataset-IIB and IIC, we randomly chose 50 voxels in each of the three sub-regions and used a lower SNR ($\text{SNR}_{outlier} = -3$ dB for Dataset-IIB, and $\text{SNR}_{outlier} = -10$ dB for Dataset-IIC) to generate the signals for those voxels. These 150 voxels serve as the outliers and the rest of the voxels are generated using $\text{SNR}_{data} = 6$ dB as Dataset-IIA. The procedure is repeated 50 times so that Dataset-IIA, IIB and IIC each contains 50 sets of data.

3.2. fMRI Dataset

The fMRI dataset consisted of nine healthy subjects. The subjects were recruited from the Pacific Parkinson's Research Centre Movement Disorders Clinic at the University of British Columbia. The study was approved by the Clinical Research Ethics Board of the University of British Columbia and the patients gave written, informed consent prior to the study. Resting state MRI examinations were performed on a Philips 3 T MRI scanner (Achieva, Philips Healthcare, Best, The Netherlands) equipped with a headcoil with eight channels. The subjects laid on their back with their eyes closed during the examination and whole brain three-dimensional $T1$-weighted images with 170 axial slices were acquired. Each functional run spanned eight minutes during which blood oxygen level dependent (BOLD) contrast echo-planar (EPI) $T2^*$-weighted images were acquired with a repetition time of 1985 ms, echo time of 37 ms and flip angle of 90°. The field of view (FOV) was set to 240 mm which included the cerebellum ventrally as well as the dorsal surface of the brain. In total 240 time-points were acquired with 36 axial slices of 3 mm thickness and 1 mm gap thickness. The matrix size was 128×128 and pixel size was 1.9 mm×1.9 mm.

The raw fMRI data were pre-processed using the pipeline described in [36]. This includes SPM-based slice timing and motion correction, isotropic reslicing and FSL (FMRIB Software Library)-derived registration. We use a linear transformation in FSL to transform the T1 anatomical image to the mean fMRI image. The transformed T1 image is then segmented with open-source Freesurfer software [37]. Despiking was accomplished with the AFNI package 3dDespike. In addition, we regressed out nuisance information from white matter, csf, and their temporal derivatives. We extracted 54 regions-of-interest (ROI) by using Freesurfer software. This particular ROI-based

14

Table 2: List of regions of interest

Region of Interest	HMAT Label
Sensorimotor Area (SMA)	ctx-lh-postcentral, L_S1, L_M1
Orbitofrontal Gyrus (OF)	ctx-lh-medialorbitofrontal, ctx-lh-lateralorbitofrontal
Cingulate gyrus (CG)	ctx-lh-caudalanteriorcingulate, ctx-lh-posteriorcingulate
Putamen	Left-putamen

segmentation method minimizes registration error especially in sub-cortical brain regions such as the putamen and hence it is favorable over manual segmentation. However, the extracted ROIs were also visually checked by experienced neurologists if needed. All data analysis were done on the unwarped images (in the native space) on a subject-by-subject basis rather than warping images into a common template. In this work, we used four ROIs from the left hemisphere of the brain namely, sensorimotor area (SMA), orbitofrontal gyrus (OF), cingulate gyrus (CG) and the putamen. The orbitofrontal gyrus included both medial and lateral orbitofrontal cortices, the cingulate gyrus included the anterior and posterior cingulate gyri and the sensorimotor area consisted of the primary motor and somatosensory cortex. The Human Motor Area Template (HMAT) labels for these four regions are listed in Table 2.

4. Results

4.1. Result on Synthetic Datasets

We applied the proposed framework on the synthetic datasets with different numbers of subROIs and the results are reported in Table 3. To compare the results generated using our proposed framework with existing methods in the literature, we also performed k-means clustering, modularity detection algorithm and spatially regularized regression model on the synthetic datasets. The k-means clustering is implemented according to [27], where at first we calculated the connectivity of the voxels within $\mathcal{V}$ with the reference ROIs X, Y and Z using Pearson's pairwise correlation coefficients, ρ. These coefficients are then transformed into Fisher's z-statistics as follows:

$$z = 0.5 \times \log \frac{1 + \rho}{1 - \rho} \qquad (11)$$

Then each voxel in $\mathcal{V}$ has a three-dimensional feature vector where each element represents the z-score between the voxel and each of the reference regions. This feature vector is used for the k-means clustering where k was set to 2 and Euclidean distance was used to cluster the ROI. For the modularity detection method [20], we constructed a undirected weighted graph where each voxel in $\mathcal{V}$ is denoted by a node in the graph, and the edge weights are calculated from the similarity matrix described in [20, 15]. We used the modularity detection algorithm developed by Newman [38] to detect communities from the generated graph.

The spatially regularized regression model is developed according to [34], where a spatially-regularized fused lasso algorithm is applied between each voxel in $\mathcal{V}$ and each reference ROI. Then adjacent voxels with similar connectivity weights are merged into one group and the process is repeated iteratively until final separation is obtained. With three reference ROIs X, Y, and Z, we got three parcellation results, and out of these three we selected the top-2 results that best match with the ground truth. To compare the outcomes from different algorithms we calculated the misclassification error percentage defined as:

$$Error = \frac{Total \ number \ of \ misclassified \ voxels}{Total \ number \ of \ voxels \ in \ \mathcal{V}} \times 100\% \qquad (12)$$

Table 3: Percentage of errors for synthetic datasets. The dataset generation procedure is repeated 50 times for each of the datasets, and the errors are reported as average error percentage over 50 datasets.

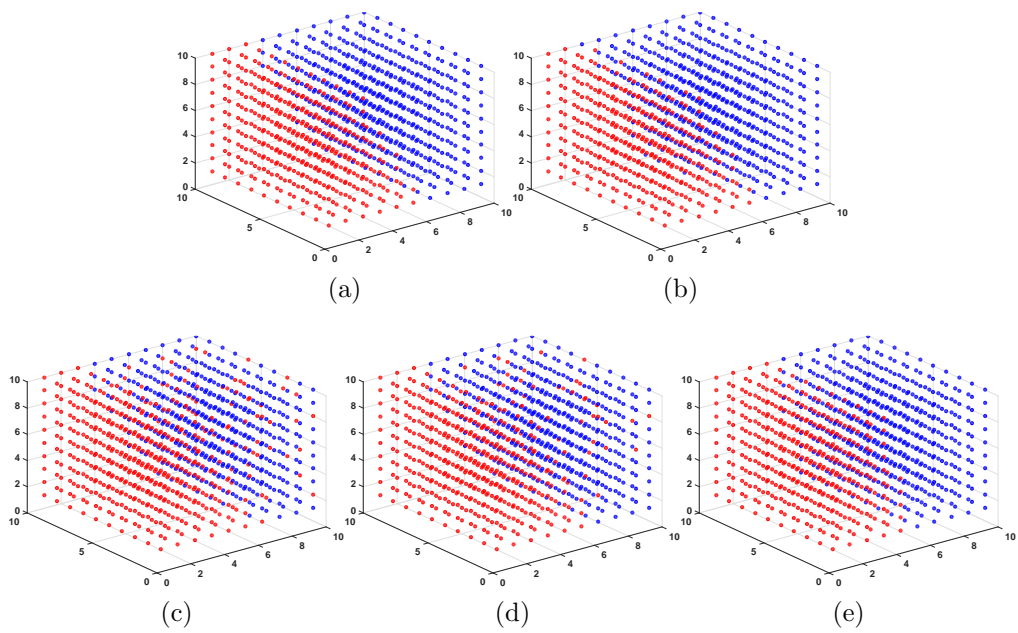|	Two subROIs			Three subROIs		
	IA	IB	IC	IIA	IIB	IIC
Proposed method	**0%**	**0.32%**	**2.50%**	**0%**	**0%**	**0.30%**
k-means clustering [27]	0%	1.50%	9.99%	0.99%	0.76%	12.35%
Modularity detection [20]	0%	0.002%	5.97%	0%	0.08%	6.13%
Spatially regularized regression [34]	2.87%	3.80%	2.90%	–	–	–

Figure 5: One example showing the typical behaviours of the of the algorithms on Dataset-IC. (a) Ground truth, (b) parcellation using the proposed framework, (c) parcellation using the k-means algorithm. (d) parcellation using the modularity maximization technique. (e) parcellation using spatially regularized regression method.

Table 3 reports the average error percentage for each of the methods on Dataset-I and II. The data generation procedure was repeated 50 times for each of the datasets and the percentage of errors reported here are average error over these 50 sets of data for each dataset. For Datasets-IA and IIA all the methods work pretty well and they correctly identified the underlying clusters. However, when we included the outlier voxels in Datasets-IB, IC, IIB and IIC, the proposed framework works better than both the k-means clustering method and modularity detection based method. The performance of the proposed framework is substantially better than k-means clustering method and modularity detection at the presence of noisy outliers for Datasets IC and IIC, where $\mathrm{SNR}_{outlier}$ = -10 dB. For Dataset-IC the proposed framework generated comparable performance with the spatially regularized regression method. Note that the spatially regularized regression method generates one parcellation result for each of the three reference ROIs, and out of these three results, in Table 3 we reported the average of the top-2 results that best match with the ground truth. In other cases the spatially regularized method generates a lot of misclassified voxels (error 5-56%), sometimes merging all the voxels into one cluster, and when the ground truth is not available it is impossible to determine which parcellation result is accurate out of these three different results. Furthermore, the parameter tuning of the regression method is challenging and time-consuming. On the other hand, the proposed framework is computationally faster and outperforms other methods even with the presence of outlier voxels. Note that the spatially regularized regression method is only defined for extracting two subROIs, and hence it can not be applied to Dataset-II.

Fig. 5 shows the performance of the algorithms on one case of Dataset-IC. As can be seen from the figure, the k-means algorithm and the modularity-based technique fail to correctly cluster the outlier voxels and hence fails to generate spatially contiguous subROIs. Fig. 6 shows another example from Dataset-IIC where the proposed frmaework outperforms other methods by correctly clustering the outlier voxels. We applied our proposed framework with different distance threshold values, T and reported the results where minimum average error is achieved. For all cases the minimum average error is achieved for larger values of T (when $T > 5$).

4.2. Result on fMRI Dataset

We applied the proposed framework in the putaminal region to parcellate it into two functional subROIs. As discussed earlier, three reference
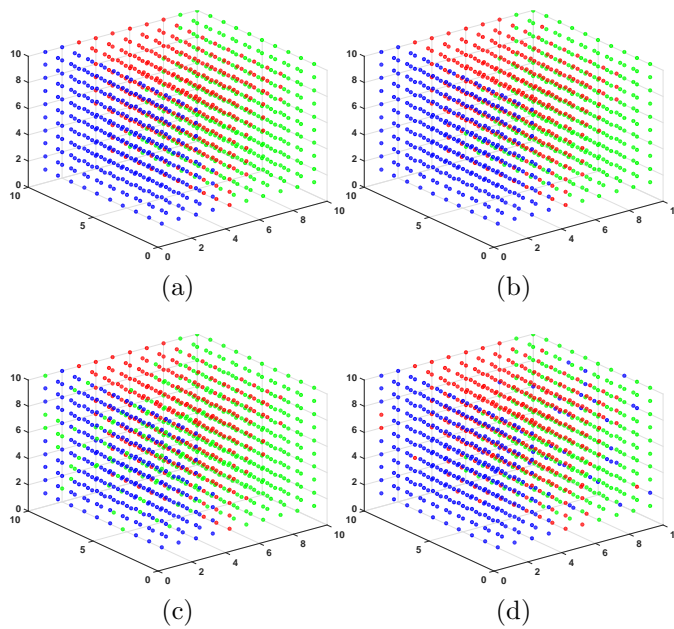
18

Figure 6: The performance of the methods on one example from Dataset-IIC where most methods fail to detect underlying subROI structure. (a) Ground truth. (b) Parcellation using the proposed framework. The proposed method detects the underlying subROIs with only a few misclassified voxels. (c) The performance of k-means algorithm on this data. (d) Parcellation result using the modularity maximization technique. The k-means algorithm and the modularity-based technique fails to correctly cluster the outlier voxels.
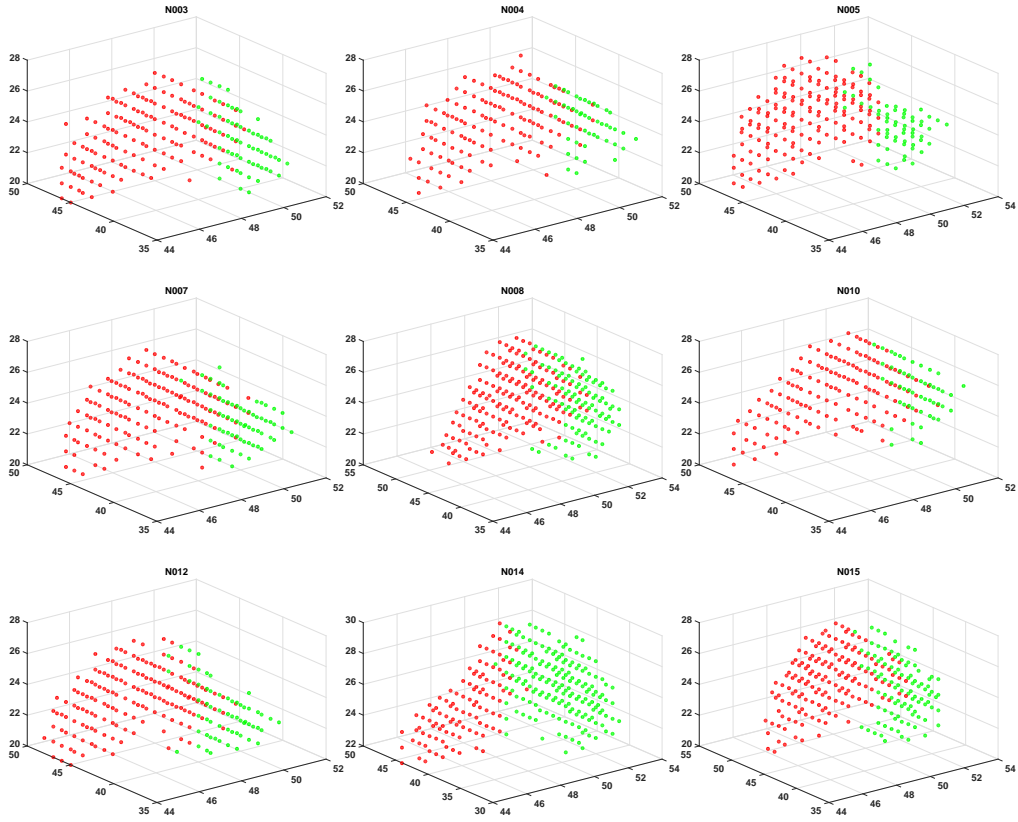
Figure 7: Putamen parcellation results using the proposed framework for nine healthy subjects. The red dots represent the dorsomedial striatum (DMS) subROI and the green dots represent the dorsolateral striatum (DLS) subROI.

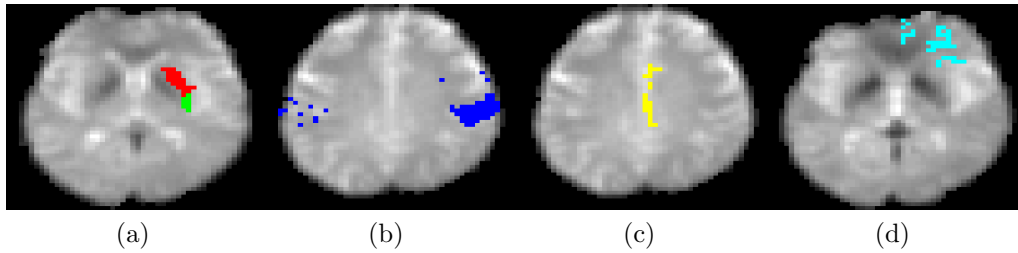(a)   (b)   (c)   (d)

Figure 8: The parcellated putamen and the reference ROIs, with a background axial fMRI image for one subject. (a) The parcellated putamen, the red region represent the dorsomedial striatum (DMS) subROI and the green region represent the dorsolateral striatum (DLS) subROI; (b) the left sensorimotor area (SMA); (c) cingulate gyrus (CG); and (d) orbitofrontal gyrus (OF) .

regions - sensorimotor area, cingulate gyrus, and orbitofrontal gyrus were considered to sub-divide the putaminal region into DLS and DMS. Among the two functional subROIs, anatomically DLS resides at the lateral part of the striatum whereas DMS lies in the medial portion. After clustering the putamen voxels using the proposed framework, we utilized this anatomical knowledge to label the clusters. We calculated the spatial location of the centroids of the generated clusters. The cluster with the laterally positioned centroid is then labeled as DLS and the other cluster is labeled as DMS. Fig. 7 shows the putamen parcellation results in the left hemisphere of the brain for nine healthy subjects with the proposed framework. The red dots denote the DMS voxels whereas the green dots represent the DLS voxels. The generated functional subROIs are spatially contiguous and nicely separated. Fig. 8 shows the parcellation result along with the reference ROIs on one axial slice for one subject. The total number of DLS and DMS voxels resulted from applying the proposed framework is shown in Fig. 9. As can be seen, in all cases but one, the total number of DMS voxels are higher than the total number of DLS voxels.
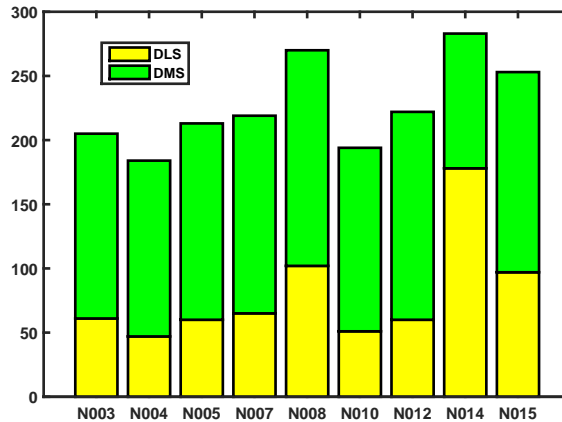

Figure 9: Bar graph of DLS and DMS voxels in left-putaminal region. The yellow bar represents the total number of DLS voxels and green bar represents the total number of DMS voxels.

To illustrate the robustness of the proposed framework in the fMRI dataset, we applied the framework on two downsampled versions of the putamen fMRI signals and compared the results. For each subject, the odd time-points ($t = 1, 3, 5, ...$) are taken to generate the first downsampled version of fMRI signals, and the even time-points ($t = 2, 4, 6, ...$) are used to generate the
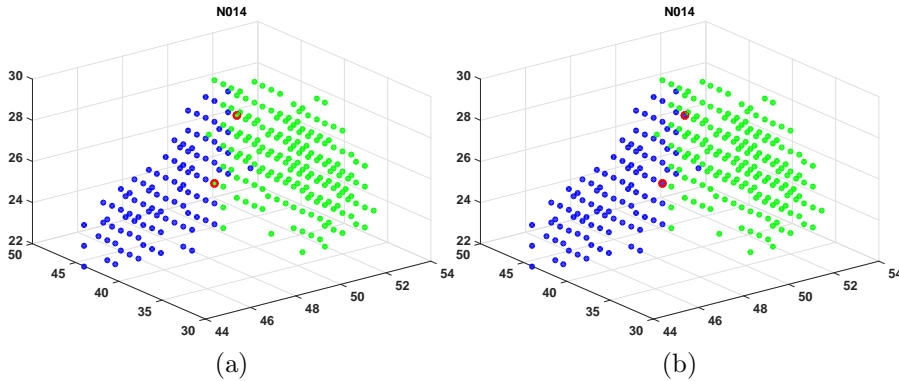
Figure 10: One example of the robustness analysis. (a) Parcellation using the odd time-points of the fMRI signals from the putamen voxels. (b) parcellation using the even time-points of the fMRI signals from the putamen voxels. The blue dots represent the dorsomedial striatum (DMS) subROI and the green dots represent the dorsolateral striatum (DLS) subROI. The voxels that belong to different clusters in these two cases are outlined with red color.

Table 4: Percentage of similarly clustered voxels (ϵ) in two downsampled fMRI datasets.

Subject	N003	N004	N005	N007	N008	N010	N012	N014	N015
Similarly clustered voxel percentage, ϵ	99.02%	100%	98.12%	100%	98.89%	98.45%	99.10%	99.29%	98.81%

second set of fMRI signals. Both these signals are then resampled to the original sampling frequency. We then applied the proposed framework separately onto these two fMRI signals and compared the clustering results. Fig. 10 illustrates one representative example of the analysis.

To compare the clustering results we define the percentage of similarly classified voxels as:

$$\epsilon = \frac{S}{N} \times 100\% \tag{13}$$

where S is the total number of voxels that belong to the same cluster for both cases, and N is the total number of voxels in putamen. This procedure is carried out for all nine subjects and over all subjects the average ϵ is found to be 99.08%. This means that over 99% voxels belong to the same cluster even when two different downsampled fMRI signals are used. Table. 4 reports the percentage of similarly clustered voxels for all the subjects. As

shown in Fig. 10, the voxels belonging to different clusters belong to the border of the two subROIs. This observation was consistent among subjects.

5. Conclusion

In this paper, we proposed a framework for parcellation of one brain ROI, a target ROI, into functional subROIs based on their inter-connectivity and intra-connectivity patterns between the target ROI and other reference brain regions. We proposed a connectivity network generation approach that takes into account the connectivity and spatial distance between voxels in the target ROI as well as their dissimilarity in connectivities with other brain reference ROIs. A community detection algorithm based on the ratio of eigenvectors of the associated adjacency matrix is then applied to sub-divide the network into several functionally connected and spatially contiguous subROIs. The framework is applied to two sets of synthetic dataset and a real fMRI dataset with nine healthy subjects. The outcomes on the synthetic datasets show that the proposed framework outperforms other literature-based methods. In particular, the proposed framework works significantly better in the presence of outliers in the data. The proposed framework is then applied to real fMRI data to sub-divide the putamen brain region into two functional subROIs, namely DLS and DMS.

Putaminal subregions, as shown here, subserve different motor functions. Typically, dorsomedial regions have been implicated in goal-directed motor performance, and more lateral regions are activated during habitual movements [25,26]. Goal-directed learning is slow, while in habitual learning, motor behavior is fast and spontaneous [39]. Repeated training of a new motor task makes the task more habitual and requires less goal-directed effort. In Parkinson's disease, the caudolateral putamen is affected early [40], and thus reduction of previously automatic movements (such as arm swing during walking) are an early sign of the disease. The early putaminal connectivity changes seen even in asymptomatic subjects with genetic mutations at risk developing Parkinson's [41] suggests that the proposed approach could assist in the development of an early imaging biomarker of the disease.

The proposed framework deviates from other methods in the literature in several aspects. First, most graph-theory based approaches only examine connectivity between the voxels in the target ROI as the only criterion for subROI parcellation. However in some cases like the putamen, the functional subROIs differ in terms of their connectivities with other brain ROIs. On the

other hand, other methods solely examine the connectivity with other brain regions, ignoring the inter-connectivity of voxels within the target ROI. Both these two connectivity factors can influence the ROI parcellation, and the proposed framework incorporates both connectivity patterns to generate a complete connectivity graph. Secondly, the proposed framework also imposes spatial continuity of subROIs, which is considered in only a few works [39, 40, 41] and often neglected in the literature [27, 31, 42]. Moreover, compared to other methods the proposed framework is not computationally intensive.

One potential limitation of the framework is the use of Euclidean distance to measure the distances between voxels in the brain. Euclidean distance may not always be appropriate for convoluted cortical regions, where other metrics such as geodesic distance may be more appropriate. However in the case of a subcortical regions such as the putamen, thalamus, etc., the Euclidean distance still seems reasonable.

The framework can be generally applied to brain ROI parcellation problems where the parcellation of the ROI depends on its connectivity with external brain ROIs, and where the final subROIs are expected to be spatially contiguous. Although the proposed framework described here is used to sub-divide a single ROI into two subROIs, this framework could be applied for any number of functional subROI extraction. One potential application of the framework can be in neurological disease-based studies where functional subROI parcellation can help understand the detection or progression of diseases. In the future, we plan to apply this framework to extract functional subROIs on a dataset of patients with Parkinson's disease, where the outcome might allow for development of novel biomarkers.

References

[1] M. P. Van Den Heuvel, H. E. H. Pol, Exploring the brain network: a review on resting-state fMRI functional connectivity, European Neuropsychopharmacology 20 (8) (2010) 519–534.

[2] R. M. Hutchison, T. Womelsdorf, E. A. Allen, P. A. Bandettini, V. D. Calhoun, et al., Dynamic functional connectivity: promise, issues, and interpretations, Neuroimage 80 (2013) 360–378.

[3] V. D. Calhoun, R. Miller, G. Pearlson, T. Adalı, The chronnectome: time-varying connectivity networks as the next frontier in fMRI data discovery, Neuron 84 (2) (2014) 262–274.

[4] A. Liu, X. Chen, M. J. McKeown, Z. J. Wang, A sticky weighted regression model for time-varying resting-state brain connectivity estimation, IEEE Transactions on Biomedical Engineering 62 (2) (2015) 501–510.

[5] M. J. Lowe, M. Dzemidzic, J. T. Lurito, V. P. Mathews, M. D. Phillips, Correlations in low-frequency BOLD fluctuations reflect cortico-cortical connections, Neuroimage 12 (5) (2000) 582–587.

[6] A. Liu, J. Li, Z. J. Wang, M. J. McKeown, A computationally efficient, exploratory approach to brain connectivity incorporating false discovery rate control, a priori knowledge, and group inference, Computational and mathematical methods in medicine 2012.

[7] S. B. Eickhoff, B. Thirion, G. Varoquaux, D. Bzdok, Connectivity-based parcellation: Critique and implications, Human brain mapping 36 (12) (2015) 4771–4792.

[8] E. Bullmore, O. Sporns, Complex brain networks: graph theoretical analysis of structural and functional systems, Nature Reviews Neuroscience 10 (3) (2009) 186–198.

[9] M. Greicius, Resting-state functional connectivity in neuropsychiatric disorders, Current opinion in neurology 21 (4) (2008) 424–430.

[10] A. Liu, X. Chen, Z. J. Wang, Q. Xu, S. Appel-Cresswell, M. J. McKeown, A genetically informed, group fMRI connectivity modeling approach: application to schizophrenia, IEEE Transactions on Biomedical Engineering 61 (3) (2014) 946–956.

[11] B. Biswal, F. Zerrin Yetkin, V. M. Haughton, J. S. Hyde, Functional connectivity in the motor cortex of resting human brain using echo-planar MRI, Magnetic resonance in medicine 34 (4) (1995) 537–541.

[12] J. Damoiseaux, S. Rombouts, F. Barkhof, P. Scheltens, C. Stam, et al., Consistent resting-state networks across healthy subjects, Proceedings of the national academy of sciences 103 (37) (2006) 13848–13853.

[13] M. D. Greicius, B. Krasnow, A. L. Reiss, V. Menon, Functional connectivity in the resting brain: a network analysis of the default mode hypothesis, Proceedings of the National Academy of Sciences 100 (1) (2003) 253–258.

[14] J. Rademacher, V. Caviness, H. Steinmetz, A. Galaburda, Topographical variation of the human primary cortices: implications for neuroimaging, brain mapping, and neurobiology, Cerebral Cortex 3 (4) (1993) 313–329.

[15] A. L. Cohen, D. A. Fair, N. U. Dosenbach, F. M. Miezin, D. Dierker, et al., Defining functional areas in individual human brains using resting functional connectivity MRI, Neuroimage 41 (1) (2008) 45–57.

[16] M. Beckmann, H. Johansen-Berg, M. F. Rushworth, Connectivity-based parcellation of human cingulate cortex and its relation to functional specialization, The Journal of neuroscience 29 (4) (2009) 1175–1190.

[17] Y. Zhang, A. Liu, S. N. Tan, M. J. McKeown, Z. J. Wang, Connectivity-based parcellation of putamen using resting state fMRI data, in: 2015 IEEE 12th International Symposium on Biomedical Imaging (ISBI), IEEE, 2015, pp. 34–37.

[18] A. Di Martino, A. Scheres, D. S. Margulies, A. Kelly, L. Q. Uddin, et al., Functional connectivity of human striatum: a resting state fMRI study, Cerebral cortex 18 (12) (2008) 2735–2747.

[19] H. BJ, S.-M. C, P. J, et al., Altered corticostriatal functional connectivity in obsessive-compulsive disorder, Archives of General Psychiatry 66 (11) (2009) 1189–1200.

[20] K. A. Barnes, A. L. Cohen, J. D. Power, S. M. Nelson, Y. B. Dosenbach, et al., Identifying basal ganglia divisions in individuals using resting-state functional connectivity MRI, Frontiers in systems neuroscience 4 (2010) 7–11.

[21] R. J. Janssen, P. Jylänki, R. P. Kessels, M. A. van Gerven, Probabilistic model-based functional parcellation reveals a robust, fine-grained subdivision of the striatum, Neuroimage 119 (2015) 398–405.

[22] C. T. Butts, Revisiting the foundations of network analysis, science 325 (5939) (2009) 414–416.

[23] T. Hedden, J. D. Gabrieli, Insights into the ageing mind: a view from cognitive neuroscience, Nature reviews neuroscience 5 (2) (2004) 87–96.

[24] K. Rubia, A. B. Smith, J. Woolley, C. Nosarti, I. Heyman, et al., Progressive increase of frontostriatal brain activation from childhood to adulthood during event-related tasks of cognitive control, Human brain mapping 27 (12) (2006) 973–993.

[25] A. J. Gruber, R. J. McDonald, Context, emotion, and the strategic pursuit of goals: interactions among multiple brain systems controlling motivated behavior, Frontiers in behavioral neuroscience 6 (2012) 50.

[26] P. Redgrave, M. Rodriguez, Y. Smith, M. C. Rodriguez-Oroz, S. Lehericy, et al., Goal-directed and habitual control in the basal ganglia: implications for Parkinson's disease, Nature Reviews Neuroscience 11 (11) (2010) 760–772.

[27] T. Kahnt, L. J. Chang, S. Q. Park, J. Heinzle, J.-D. Haynes, Connectivity-based parcellation of the human orbitofrontal cortex, The Journal of Neuroscience 32 (18) (2012) 6240–6250.

[28] R. Baumgartner, G. Scarth, C. Teichtmeister, R. Somorjai, E. Moser, Fuzzy clustering of gradient-echo functional MRI in the human visual cortex. Part I: Reproducibility, Journal of Magnetic Resonance Imaging 7 (6) (1997) 1094–1101.

[29] L. Wang, Q. Liu, H. Li, D. Hu, Functional connectivity-based parcellation of human medial frontal cortex via maximum margin clustering,

in: International Conference on Intelligent Science and Intelligent Data Engineering, Springer, 2012, pp. 306–312.

[30] V. Kiviniemi, J.-H. Kantola, J. Jauhiainen, A. Hyvärinen, O. Tervonen, Independent component analysis of nondeterministic fMRI signal sources, Neuroimage 19 (2) (2003) 253–260.

[31] A. Mezer, Y. Yovel, O. Pasternak, T. Gorfine, Y. Assaf, Cluster analysis of resting-state fMRI time series, Neuroimage 45 (4) (2009) 1117–1125.

[32] B. Thirion, S. Dodel, J.-B. Poline, Detection of signal synchronizations in resting-state fMRI datasets, Neuroimage 29 (1) (2006) 321–327.

[33] X. Shen, X. Papademetris, R. T. Constable, Graph-theory based parcellation of functional subunits in the brain from resting-state fMRI data, Neuroimage 50 (3) (2010) 1027–1035.

[34] Y. Zhang, A. Liu, S. N. Tan, M. J. McKeown, Z. J. Wang, Connectivity-based parcellation of functional SubROIs in putamen using a sparse spatially regularized regression model, Biomedical Signal Processing and Control 27 (2016) 174–183.

[35] J. Jin, Fast community detection by SCORE, The Annals of Statistics 43 (1) (2015) 57–89.

[36] J. Chen, S. J. Palmer, A. R. Khan, M. J. McKeown, M. F. Beg, Freesurfer-initialized large deformation diffeomorphic metric mapping with application to Parkinson's disease, in: SPIE Medical Imaging, International Society for Optics and Photonics, 2009, pp. 725931–725931.

[37] Freesurfer, `http://freesurfer.net/`.

[38] M. E. Newman, Modularity and community structure in networks, Proceedings of the national academy of sciences 103 (23) (2006) 8577–8582.

[39] P. Bellec, V. Perlbarg, S. Jbabdi, M. Pélégrini-Issac, J.-L. Anton, J. Doyon, H. Benali, Identification of large-scale networks in the brain using fMRI, Neuroimage 29 (4) (2006) 1231–1243.

[40] B. Thirion, G. Flandin, P. Pinel, A. Roche, P. Ciuciu, J.-B. Poline, Dealing with the shortcomings of spatial normalization: Multi-subject

parcellation of fMRI datasets, Human brain mapping 27 (8) (2006) 678–693.

[41] R. C. Craddock, G. A. James, P. E. Holtzheimer III, X. P. Hu, H. S. Mayberg, A whole brain fMRI atlas generated via spatially constrained spectral clustering, Human brain mapping 33 (8) (2012) 1914–1928.

[42] M. Van Den Heuvel, R. Mandl, H. H. Pol, Normalized cut group clustering of resting-state fMRI data, PloS one 3 (4) (2008) e2001.